Abstracta

Ano XXIV - N. 03

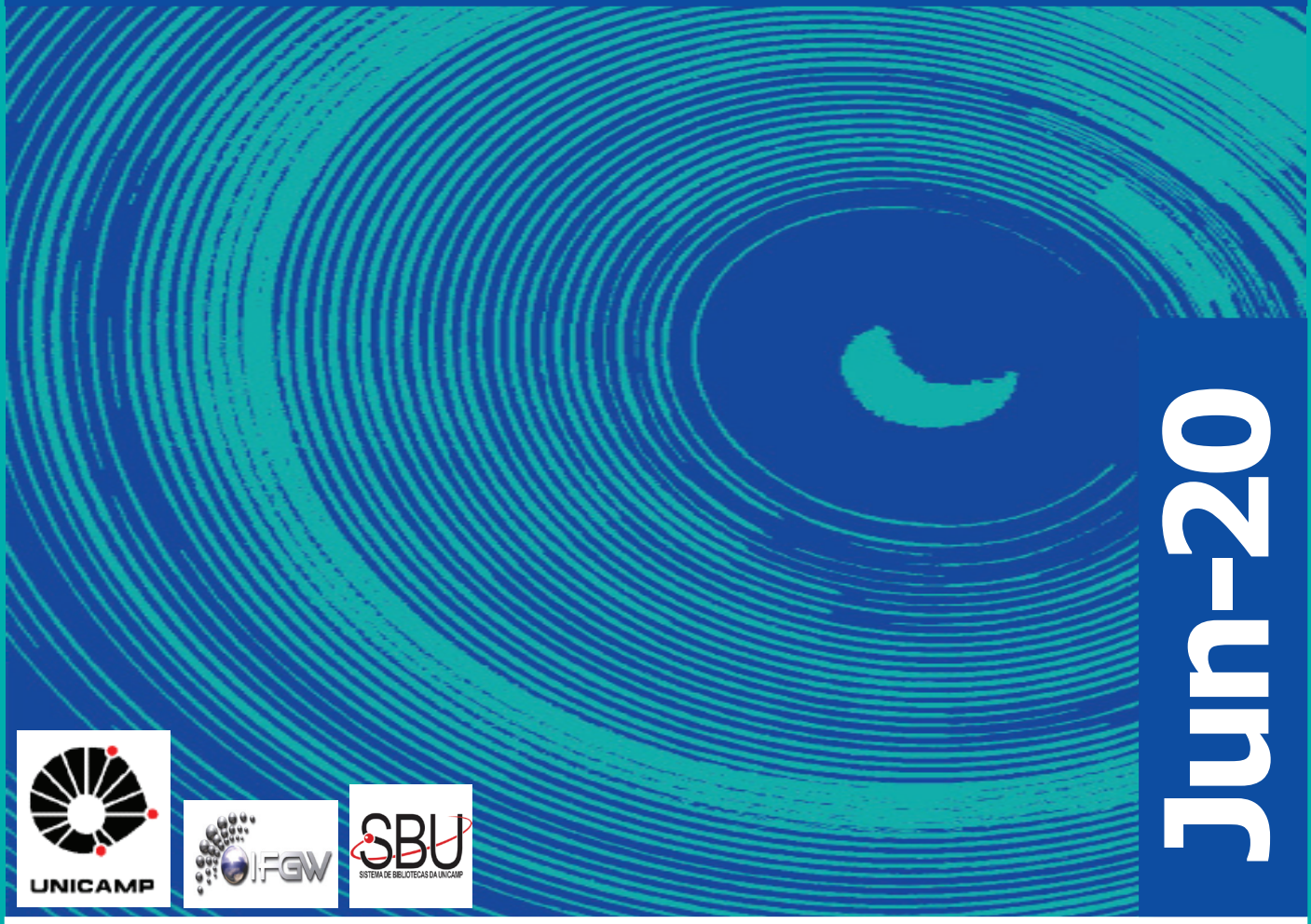

Jun-20

Artigos publicados - P085-2020 à P144-2020

Patentes do IFGW - Pa001-2020

Defesas de Dissertações do IFGW - D007-2020 à D010-2020

Defesas de Teses do IFGW - T007-2020

Defesas de Teses do PECIM - Pe002-2020 à Pe003-2020

Artigos publicados

[P085-2020] "A complete simulation of the X-ARAPUCA device for detection of scintillation photons"

Paulucci, L.; Marinho, F.; **Machado, A. A.*; Segreto, E.***

The concept of the ARAPUCA device is relatively new and involves increasing the effective area for photon collection of SiPMs by the use of a box with highly reflective internal walls, wavelength shifters, and a dichroic filter to allow the light to enter the box and not the leave it. There were a number of tests showing the good performance of this device. Recently an improvement on the original design was proposed: the inclusion of a WLS bar inside the box to guide photons more efficiently to the SiPMs. We present a full simulation of the device using Geant4. We have included all the material properties that are available in the literature and the relevant detailed properties for adequate photon propagation available in the framework. Main results include estimates of detection efficiency as a function of the number, shape, and placing of SiPMs, width of the WLS bar, its possible attenuation, and the existence of a gap between the bar and the SiPMs. Improvement on the efficiency with respect to the original ARAPUCA design is 15-40%. The ARAPUCA simulation has been validated in a number of experimental setups and is a useful tool to help making design choices for future experiments devices.

JOURNAL OF INSTRUMENTATION 15[1], C01047, 2020. DOI: 10.1088/1748-0221/15/01/C01047

[P086-2020] "A multi-dimensional search for new heavy resonances decaying to boosted WW, WZ, or ZZ boson pairs in the dijet final state at 13TeV"

Sirunyan, A. M.; Tumasyan, A.; Adam, W.; **Chinellato, J. A.*; Tonelli Manganote, E. J.***; et. al.; CMS Collaboration

A search in an all-jet final state for new massive resonances decaying to WW, WZ, or ZZ boson pairs using a novel analysis method is presented. The analysis is performed on data corresponding to an integrated luminosity of 77.3 fb(-1) recorded with the CMS experiment at the LHC at a centre-of-mass energy of 13TeV. The search is focussed on potential narrow-width resonances with masses above 1.2TeV, where the decay products of each W or Z boson are expected to be collimated into a single, large-radius jet. The signal is extracted using a three--dimensional maximum likelihood fit of the two jet masses and the dijet invariant mass, yielding an improvement in sensitivity of up to 30% relative to previous search methods. No excess is observed above the estimated standard model background. In a heavy vector triplet model, spin-1 Z' and W' resonances with masses below 3.5 and 3.8TeV, respectively, are excluded at 95% confidence level. In a bulk graviton model, upper limits on cross sections are set between 27 and 0.2 fb for resonance masses between 1.2 and 5.2TeV, respectively. The limits presented in this paper are the best to date in the dijet final state.

EUROPEAN PHYSICAL JOURNAL C 80[3], 237, 2020. DOI: 10.1140/epjc/s10052-020-7773-5

[P087-2020] "A search for the standard model Higgs boson decaying to charm quarks"

Sirunyan, A. M.; Tumasyan, A.; Adam, W.; **Chinellato, J. A.*; Tonelli Manganote, E. J.***; et. al.; CMS Collaboration

A direct search for the standard model Higgs boson, H, produced in association with a vector boson, V (W or Z), and decaying to a charm quark pair is presented. The search uses a data set of proton-proton collisions corresponding to an integrated luminosity of 35.9 fb(-1), collected by the CMS experiment at the LHC in 2016, at a centre-of-mass energy of 13 TeV. The search is carried out in mutually exclusive channels targeting specific decays of the vector bosons: W -> l nu, Z -> ll, and Z -> nu nu, where l is an electron or a muon. To fully exploit the topology of the H boson decay, two strategies are followed. In the first one, targeting lower vector boson transverse momentum, the H boson candidate is reconstructed via two resolved jets arising from the two charm quarks from the H boson decay. A second strategy identifies the case where the two charm quark jets from the H boson decay merge to form a single jet, which generally only occurs when the vector boson has higher transverse momentum. Both strategies make use of novel methods for charm jet identification, while jet substructure techniques are also exploited to suppress the background in the merged-jet topology. The two analyses are combined to yield a 95% confidence level observed (expected) upper limit on the cross section sigma(VH) corresponding to 70 (37) times the standard model prediction.

JOURNAL OF HIGH ENERGY PHYSICS 3[131], 2020. DOI: 10.1007/JHEP03(2020)131

[P088-2020] "Agarose-based structured optical fibre"

Fujiwara, E.; **Cabral, T. D.*;** Sato, M.; Oku, H.; **Cordeiro, C. M. B.***

Biocompatible and resorbable optical fibres emerge as promising technologies for in vivo applications like imaging, light delivery for phototherapy and optogenetics, and localised drug--delivery, as well as for biochemical sensing, wherein the probe can be implanted and then completely absorbed by the organism. Biodegradable waveguides based on glasses, hydrogels, and silk have been reported, but most of these devices rely on complex fabrication procedures. In this sense, this paper proposes a novel structured optical fibre made of agarose, a transparent, edible material used in culture media and tissue engineering. The fibre is obtained by pouring food-grade agar into a mould with stacked rods, forming a solid core surrounded by air holes in which the refractive index and fibre geometry can be tailored by choosing the agarose solution composition and mould design, respectively. Besides exhibiting practical transmittance at 633nm in relation to other hydrogel waveguides, the fibre is also validated for chemical sensing either by detecting volume changes due to agar swelling/dehydration or modulating the transmitted light by inserting fluids into the air holes. Therefore, the proposed agarose-based structured optical fibre is an easy-to-fabricate, versatile technology with possible applications for medical imaging and in vivo biochemical sensing.

SCIENTIFIC REPORTS 10[1], 2020. DOI: 10.1038/s41598-020-64103-3

[P089-2020] "Anisotropic superconductivity mediated by ferroelectric fluctuations in cubic systems with spin-orbit coupling"

Gastiasoro, M. N.; **Trevisan, T. V.***; Fernandes, R. M.

Motivated by the experimental observation that superconductivity in bulk doped SrTiO3 is enhanced as a putative ferroelectric quantum critical point (FE-QCP) is approached, we study the pairing instability of a cubic system in which electrons exchange low-energy ferroelectric fluctuations. Instead of the gradient coupling to the lattice distortion associated with ferroelectricity, we consider direct coupling between the electrons and the bosonic ferroelectric field that appears in the presence of spin-orbit coupling. Working in the weak-coupling regime, we find that the pairing interaction is dominated by the soft transverse optical (TO)

mode, resulting in a T-c enhancement upon approaching the FE--QCP. Focusing on even-parity states, we find that although the s-wave state always wins, states with higher Cooper-pair angular momentum become close competitors as the TO mode softens. We show that the cubic anisotropy of the FE fluctuations mixes the s-wave and g-wave states, resulting in a characteristic anisotropy of the gap function. The gap anisotropy behaves nonmonotonically as the FE-QCP is approached: upon decreasing the TO mode frequency, the gap anisotropy first changes sign and then increases in magnitude. We discuss the possible applications of our results to the superconducting state of SrTiO3.

PHYSICAL REVIEW B101[17], 174501, 2020. DOI: 10.1103/PhysRevB.101.174501

[P090-2020] "Atomistic Simulation of Nanoindentation of Ice I-h"

Santos-Florez, P. A.*; Ruestes, C. J.; **Koning, M. de***

Using molecular dynamics simulations, we study the nanoindentation response of the ice I-h basal surface using two popular water models, namely, the all-atom TIP4P/Ice potential and the coarse-grained mW model. In particular, we consider two markedly different temperatures at which a quasi-liquid layer (QLL) is or is not present. We discuss loading curves, hardness estimates, deformation mechanisms, and residual imprints, considering the effect of the QLL, indenter size, and penetration rate. At very low temperatures, in the absence of a QLL, both potentials produce similar loading curves and deformation mechanisms. Close to the melting temperature, however, important differences were found, including deviations in the QLL thickness and fraction as well as the presence of a competition between pressure-induced melting and recrystallization events. Nevertheless, both potentials exhibit similar deformation mechanisms and steady-state hardness estimates that are consistent with experimental data. In addition to contributing to the discussion regarding the interpretation of experimental AFM loading curves, the present results provide valuable information concerning the simulation of contact problems involving ice and the behavior of these two popular water models under such circumstances.

JOURNAL OF PHYSICAL CHEMISTRY C 124[17], 9329-9336, 2020. DOI: 10.1021/acs.jpcc.0c00255

[P091-2020] "Band structure engineering in strain-free GaAs mesoscopic systems"

Gordo, V. O.*; Rodrigues, L. N.; Knopper, F.; **Garcia Jr, A. J.*; Iikawa, F.*; Couto Jr, O. D. D.*; Deneke, C.***

We investigate the optical properties of strain-free mesoscopic GaAs/AlxGa1 - xAs structures (MGS) coupled to thin GaAs/AlxGa1 - xAs quantum wells (QWs) with varying Al content (x). We demonstrate that quenching the QW emission by controlling the band crossover between AlGaAs (X-point) and GaAs (Gamma-point) gives rise to long carrier lifetimes and enhanced optical emission from the MGS. For x = 0.33, QW and MGS show typical type-I band alignment with strong QW photoluminescence emission and much weaker sharp recombination lines from the MGS localized exciton states. For x >= 0.50, the QW emission is considerably quenched due to the change from type-I to type-II structure while the MGS emission is enhanced due to carrier injection from the QW. For x >= 0.70, we observe PL quenching from the MGS higher energy states also due to the crossover of X and Gamma bands, demonstrating spectral filtering of the MGS emission. Time--resolved measurements reveal two recombination processes in the MGS emission dynamics. The fast component depends mainly on the X - Gamma mixing of the MGS states and can be increased from 0.3 to 2.5 ns by changing the Al content. The slower component, however, depends on the X - Gamma mixing of the QW states and is associated to the carrier injection rate from the QW reservoir into the MGS structure. In this way, the independent tuning of X - Gamma mixing in QW and MGS states allows us to manipulate recombination rates in the MGS as well as to make carrier injection and light extraction more efficient.

NANOTECHNOLOGY 31[25], 255202, 2020. DOI: 10.1088/1361-6528/ab7d74

[P092-2020] "Computed tomography-based skeletal segmentation for quantitative PET metrics of bone involvement in multiple myeloma"

Takahashi, M. E. S.*; Mosci, C.; Souza, E. M.; Brunetto, S. Q.; de Souza, C.; Pericole, F. V.; Lorand-Metze, I.; Ramos, C. D.

Purpose: Quantifications in nuclear medicine are occasionally limited by the lack of standardization for defining volumes of interest (VOIs) on functional images. In the present article, we propose the use of computed tomography (CT)-based skeletal segmentation to determine anatomically the VOI in order to calculate quantitative parameters of fluorine 18 fluorodeoxyglucose (F-18-FDG) PET/CT images from patients with multiple myeloma. Methods: We evaluated 101 whole-body F-18-FDG PET/CTs of 58 patients with multiple myeloma. An initial subjective visual analysis of the PET images was used to classify the bone involvement as negative/mild, moderate, or marked. Then, a fully automated CT-based segmentation of the skeleton was performed on PET images. The maximum, mean, and SD of the standardized uptake values (SUVmax, SUVmean, and SDSUV) were calculated for bone tissue and compared with the visual analysis. Results: Forty-five (44.5%), 32 (31.7%), and 24 (23.8%) PET images were, respectively, classified as negative/mild, moderate, or marked bone involvement. All quantitative parameters were significantly related to the visual assessment of bone involvement. This association was stronger for the SUVmean [odds ratio (OR): 10.52 (95% confidence interval (CI), 5.68-19.48); P < 0.0001] and for the SDSUV [OR: 5.58 (95% CI, 3.31-9.42); P < 0.001) than for the SUVmax [OR: 1.01 (95% CI, 1.003-1.022); P = 0.003]. Conclusion: CT-based skeletal segmentation allows for automated and therefore reproducible calculation of PET quantitative parameters of bone involvement in patients with multiple myeloma. Using this method, the SUVmean and its respective SD correlated better with the visual analysis of F-18-FDG PET images than SUVmax. Its value in staging and evaluating therapy response needs to be evaluated.

NUCLEAR MEDICINE COMMUNICATIONS 41[4], 377-382, 2020. DOI: 10.1097/MNM.0000000000001165

[P093-2020] "Constraints on the chi(c1)versus chi(c2) Polarizations in Proton-Proton Collisions at root s=8 TeV"

Sirunyan, A. M.; Tumasyan, A.; Adam, W.; **Chinellato, J. A.*; Tonelli Manganote, E. J.*;** et. al.; CMS Collaboration

The polarizations of promptly produced chi(c1) and chi(c2) mesons are studied using data collected by the CMS experiment at the LHC, in proton-proton collisions at root s = 8 TeV. The chi(c) states are reconstructed via their radiative decays chi(c) -> J/psi gamma, with the photons being measured through conversions to e(+)e(-), which allows the two states to be well resolved. The polarizations are measured in the helicity frame, through the analysis of the chi(c2) to chi(c1) yield ratio as a function of the polar or azimuthal angle of the positive muon emitted in the J/psi -> mu(+)mu(-) decay, in three bins of J/psi transverse momentum. While no differences are seen between the two states in terms of azimuthal decay angle distributions, they are observed to have significantly different polar anisotropies.

The measurement favors a scenario where at least one of the two states is strongly polarized along the hclicity quantization axis, in agreement with nonrelativistic quantum chromodynamics predictions. This is the first measurement of significantly polarized quarkonia produced at high transverse momentum.

PHYSICAL REVIEW LETTERS 124[16], 162002, 2020. DOI: 10.1103/PhysRevLett.124.162002

[P094-2020] "Design and construction of a new detector to measure ultra-low radioactive-isotope contamination of argon"

Aalseth, C. E.; Abdelhakim, S.; Acerbi, F.; **Machado, A. A.*; Segreto, E.***; et. al.; DarkSide-20k Collaboration

Large liquid argon detectors offer one of the best avenues for the detection of galactic weakly interacting massive particles (WIMPs) via their scattering on atomic nuclei. The liquid argon target allows exquisite discrimination between nuclear and electron recoil signals via pulse-shape discrimination of the scintillation signals. Atmospheric argon (AAr), however, has a naturally occurring radioactive isotope, Ar-39, a beta emitter of cosmogenic origin. For large detectors, the atmospheric Ar-39 activity poses pile-up concerns. The use of argon extracted from underground wells, deprived of Ar-39, is key to the physics potential of these experiments. The DarkSide-20k dark matter search experiment will operate a dual-phase time projection chamber with 50 tonnes of radio-pure underground argon (UAr), that was shown to be depleted of Ar-39 with respect to AAr by a factor larger than 1400. Assessing the Ar-39 content of the UAr during extraction is crucial for the success of DarkSide-20k, as well as for future experiments of the Global Argon Dark Matter Collaboration (GADMC). This will be carried out by the DArT in ArDM experiment, a small chamber made with extremely radio-pure materials that will be placed at the centre of the ArDM detector, in the Canfranc Underground Laboratory (LSC) in Spain. The ArDM LAr volume acts as an active veto for background radioactivity, mostly gamma-rays from the ArDM detector materials and the surrounding rock. This article describes the DArT in ArDM project, including the chamber design and construction, and reviews the background required to achieve the expected performance of the detector.

JOURNAL OF INSTRUMENTATION 15[2], P02024, 2020. DOI: 10.1088/1748-0221/15/02/P02024

[P095-2020] "Double Chooz theta(13) measurement via total neutron capture detection"

de Kerret, H.; Abrahao, T.; Almazan, H.; **Gonzalez, L. F. G.*; Kemp, E.***; et. al.; Double Chooz Collaboration

Neutrinos were assumed to be massless particles until the discovery of the neutrino oscillation process. This phenomenon indicates that the neutrinos have non-zero masses and the mass eigenstates (nu(1), nu(2), nu(3)) are mixtures of their flavour eigenstates (nu(e), nu(mu), nu(tau)). The oscillations between different flavour eigenstates are described by three mixing angles (theta(12), theta(23), theta(13)), two differences of the squared neutrino masses of the nu(2)/nu(1) and nu(3)/nu(1) pairs and a charge conjugation parity symmetry violating phase delta(CP). The Double Chooz experiment, located near the Chooz Electricite de France reactors, measures the oscillation parameter theta(13) using reactor neutrinos. Here, the Double Chooz collaboration reports the measurement of the mixing angle theta(13) with the new total neutron capture detection technique from the full data set, yielding sin(2)(2 theta(13)) = 0.105 +/- 0.014. This measurement exploits the multidetector configuration, the isoflux baseline and data recorded when the reactors were switched off. In addition to the neutrino mixing angle measurement, Double Chooz provides a precise measurement of the reactor neutrino flux, given by the mean cross-section per fission <sigma(f)& rang; = (5.71 +/- 0.06) x 10(-43) cm(2) per fission, and reports an empirical model of the distortion in the reactor neutrino spectrum. The Double Chooz collaboration reports the neutrino oscillation parameter theta(13) from a measurement of the disappearance of reactor anti--electron neutrinos with the total neutron capture technique.

NATURE PHYSICS 16[5], 558-+, 2020. DOI: 10.1038/s41567-020-0831-y

[P096-2020] "Effective model for the A(2g) Raman signal in URu2Si2"

Farias, C. S. de*; Measson, M. A.; Ferraz, A.; Burdin, S.

We propose an effective model to describe the A(2g) signal in Raman scattering experiments in the URu2Si2 compound. We follow the scheme proposed earlier by D. V. Khveshchenko and P. B. Wiegmann [Phys. Rev. Lett. 73, 500 (1994)] to calculate the A(2g) scattering vertex. We extract the imaginary part of the two-point current-current correlation function and compare it directly with the Raman response. We obtain an inelastic peak at the A(2g) channel owing to the interplay between a local staggered ordering and a possible quantum spin liquid behavior. Our results offer an explanation for the electronic Raman scattering experiments at the hidden order phase in the URu2Si2 compound [Buhot et al., Phys. Rev. Lett.. 113, 266405 (2014)].

PHYSICAL REVIEW B 101[20], 205114, 2020. DOI: 10.1103/PhysRevB.101.205114

[P097-2020] "Effects of cold SF6 plasma treatment on a--C:H, polypropylene and polystyrene"

Amorim, M. K. M.; Rangel, E. C.; **Landers, R.***; Durrant, S. F.

The effects of cold SF6 plasma treatment on amorphous hydrogenated carbon (FA), polypropylene (PP) and polystyrene (PS) were investigated as functions of gas pressure and applied power. An anticipated increase in hydrophobicity was confirmed by the greater water contact angles, theta, observed after all the treatments. Under the best conditions theta was increased by 50.8 degrees, 57.2 degrees and 21 degrees, respectively. A rise and fall in. was observed as the pressure of SF6 was increased, this trend being most consistent for FA. Although the plasma treatments caused some changes in surface roughness, measured using profilometry, there were no clear correlations between this parameter and.. As revealed by Energy Dispersive X-ray Spectroscopy (EDS) and X-ray Photoelectron Spectroscopy (XPS), the treated surfaces were fluorinated. As the degree of fluorination under optimal conditions was 2.2 at.%, 10.4 at.% and 36.3 at.% for the FA, PP and PS, respectively, this factor was not alone responsible for the observed increases in.. Sulfur was attached to the surface of all the treated samples. The relative surface carbon content was reduced by the treatments. The main causes of the changes in theta upon treatment were the induced compositional and structural changes. Ageing for ten days caused a typical decrease in theta of similar to 10 degrees, probably caused by rotation of hydrophobic surface groups into the surface.

SURFACE & COATINGS TECHNOLOGY 385[125398], 2020. DOI: 10.1016/j.surfcoat.2020.125398

[P098-2020] "Effects of Fe substitution on Mn2Sn alloy on its structural, magnetic and magnetocaloric properties"

Felez, M. R.*; Monteiro, J. C. B.*; de Florio, D. Z.; **Gandra, F. C. G.***; Gama, S.

The effects of Fe substitution on Mn site of Mn2Sn compound was investigated by means of scanning electron microscopy with X-ray energy dispersive spectrometer, X-ray diffraction, magnetization and magnetocaloric measurements. The produced Mn2-yFeySn series (0.50 <= y <= 1.75) presented two phases, a major non-stoichiometric Mn2-xSn and a minor Mn3Sn, respectively, with Fe content replacing Mn in each phase. The lattice parameters a and c of Mn2-xSn and Mn3Sn phases decrease approximately linearly with Fe concentration while their transition temperatures increase covering a wide temperature range from 177 K to 546 K (major phase T-C1) and 260 K to 704 K (minor phase T-C2) resulting in alloys with two distinct values of T-C. The magnetization measurements show a ferromagnetic coupling and saturation magnetization increases along the series. The heat flux analyses determined second order of magnetic transitions and magnetocaloric effect was calculated with vertical bar Delta S vertical bar around 1 J/kg.K. The cooling power was estimated in 85 J/kg. Both values were for mu(0)Delta H = 2 T. Thereby, for technological devices which have their efficient improved using layered materials, Mn2-yFeySn alloys are valid candidates since the association of its properties allow to yield a powerful magnetic and magnetocaloric material, and, besides, they are low cost, non-toxic, absent of rare-earth and easy to manufacture.

JOURNAL OF MAGNETISM AND MAGNETIC MATERIALS 505[166676], 2020. DOI: 10.1016/j.jmmm.2020.166676

[P099-2020] "Evidence for WW production from double--parton interactions in proton-proton collisions at root s=13 TeV"

Sirunyan, A. M.; Tumasyan, A.; Adam, W.; **Chinellato, J. A.*; Tonelli Manganote, E. J.*;** et. al.; CMS Collaboration

A search forWWproduction from double-parton scattering processes using same-charge electron-muon and dimuon events is reported, based on proton-proton collision data collected at a center-of-mass energy of 13 TeV. The analyzed data set corresponds to an integrated luminosity of 77.4 fb-1, collected using the CMS detector at the LHC in 2016 and 2017. Multivariate classifiers are used to discriminate between the signal and the dominant background processes. A maximum likelihood fit is performed to extract the signal cross section. This leads to the first evidence for WW production via double-parton scattering, with a significance of 3.9 standard deviations. The measured inclusive cross section is 1.41 +/- 0.28 (stat) +/- 0.28 (syst) pb.

EUROPEAN PHYSICAL JOURNAL C 80[1], 41, 2020. DOI: 10.1140/epjc/s10052-019-7541-6

[P100-2020] "Evidence of rescattering effect in Pb-Pb collisions at the LHC through production of K*(892)(0) and phi(1020) mesons"

Acharya, S.; Acosta, F. T.; Adam, J.; **Albuquerque, D. S. D.*; Chinellato, D. D.*; De Souza, R. D.*; Takahashi, J.***; et al. ALICE Collaboration

Measurements of K*(892)(0) and phi(1020) resonance production in Pb-Pb and pp collisions at root s(NN) = 5.02 TeV with the ALICE detector at the Large Hadron Collider are reported. The resonances are measured at midrapidity (vertical bar y vertical bar < 0.5) via their hadronic decay channels and the transverse momentum (p(T)) distributions are obtained for various collision centrality classes up to p(T) = 20 GeV/c. The p(T)-integrated yield ratio K*(892)(0)/K in Pb-Pb collisions shows significant suppression relative to pp collisions and decreases towards more central collisions. In contrast, the phi(1020)/K ratio does not show any suppression. Furthermore, the measured K*(892)(0)/K ratio in central Pb--Pb collisions is significantly suppressed with respect to the expectations based on a thermal model calculation, while the phi(1020)/K ratio agrees with the model prediction. These measurements are an experimental demonstration of rescattering of K*(892)(0) decay products in the hadronic phase of the collisions. The K*(892)(0)/K yield ratios in Pb-Pb and pp collisions are used to estimate the time duration between chemical and kinetic freeze-out, which is found to be similar to 4-7 fm/c for central collisions. The p(T)-differential ratios of K*(892)(0)/K, phi(1020)/K, K*(892)(0)/pi, phi(1020)/pi, p/K*(892)(0) and p/phi(1020) are also presented for Pb-Pb and pp collisions at root s(NN) = 5.02 TeV. These ratios show that the rescattering effect is predominantly a low-p(T) phenomenon.

PHYSICS LETTERS B 802[135225], 2020. DOI: 10.1016/j.physletb.2020.135225

[P101-2020] "Exploration of jet substructure using iterative declustering in pp and Pb-Pb collisions at LHC energies"

Acharya, S.; Acosta, F. T.; Adam, J.; **Albuquerque, D. S. D.*; Chinellato, D. D.*; De Souza, R. D.*; Takahashi, J.***; et. al.; ALICE Collaboration

The ALICE collaboration at the CERN LHC reports novel measurements of jet substructure in pp collisions at root s = 7 TeV and central Pb-Pb collisions at root s(NN) = 2.76 TeV. Jet substructure of track-based jets is explored via iterative declustering and grooming techniques. We present the measurement of the momentum sharing of two-prong substructure exposed via grooming, the z(g), and its dependence on the opening angle, in both pp and Pb-Pb collisions. We also present the measurement of the distribution of the number of branches obtained in the iterative declustering of the jet, which is interpreted as the number of its hard splittings. In Pb-Pb collisions, we observe a suppression of symmetric splittings at large opening angles and an enhancement of splittings at small opening angles relative to pp collisions, with no significant modification of the number of splittings. The results are compared to predictions from various Monte Carlo event generators to test the role of important concepts in the evolution of the jet in the medium such as colour coherence.

PHYSICS LETTERS B 802[135227], 2020. DOI: 10.1016/j.physletb.2020.135227

[P102-2020] "Extreme and high synchrotron peak blazars beyond 4FGL: The 2BIGB gamma-ray catalogue"

Arsioli, B.*; Chang, Y-L; Musiimenta, B.

This paper presents the results of a gamma-ray likelihood analysis over all the extreme and high synchrotron peak blazars (EHSP and HSP) from the 3HSP catalogue. We investigate 2013 multifrequency positions under the eyes of Fermi Large Area Telescope, considering 11 yr of observations in the energy range between 500MeV and 500 GeV, which results in 1160 gamma-ray signatures detected down to the TS = 9 threshold. The detections include 235 additional sources concerning the Fermi Large Area Telescope Fourth Source Catalog (4FGL), all confirmed via high-energy TS (Test Statistic) maps, and represent an improvement of similar to 25 per cent for the number of EHSP and HSP currently described in gamma--rays. We build the gamma-ray spectral energy distribution (SED) for all the 1160 2BIGB sources, plot the corresponding gamma-ray logN-logS, and measure their total contribution to the extragalactic gamma-ray background, which reaches up to similar to 33 per cent at 100 GeV. Also, we show that the gamma-ray detectability improves according to the synchrotron peak flux as represented by the figure of merit parameter,

and note that the search for TeV peaked blazars may benefit from considering HSP and EHSP as a whole, instead of EHSPs only. The 2BIGB acronym stands for 'Second Brazil-ICRANet Gamma--ray Blazars' catalogue, and all the broad-band models and SED data points will be available on public data repositories (OpenUniverse, GitHub, and Brazilian Science Data Center-BSDC).

MONTHLY NOTICES OF THE ROYAL ASTRONOMICAL SOCIETY 493[2], 2438-2451, 2020. DOI: 10.1093/mnras/staa368

[P103-2020] "Fractal analysis of the formation process and morphologies of hyaluronan/chitosan nanofilms in layer-by--layer assembly"

Hernandez-Montelongo, J.*; Nascimento, V. F.; Hernandez--Montelongo, R.; Beppu, M. M.; **Cotta, M. A.***

In the last decade, hyaluronan (HA, polyanion) and chitosan (CHI, polycation) biopolymers have been assembled by layer-by-layer (LbL) for the synthesis of antibacterial coatings. As electrostatic interactions are the main driving force for the formation of LbL films, pH and ionic strength (IS) are important critical variables of synthesis. In this context, we used surface fractal analysis of HA/CHI films to characterize the growth process for different bilayers obtained with two pH (5 and 3) and IS values (0 and 0.1 M NaCl). Our results showed that the HA/CHI assembling is mainly affected by changes in the pH than IS. Fractal dimension (D-f) of pH 5 series presented values similar to 2.2, indicating that irregularities from the initial random adsorption process are minimized. However, when pH decreased to 3, D-f increases up to similar to 2.5, suggesting a transition to diffusion-limited aggregation.

POLYMER 191[122283], 2020. DOI: 10.1016/j.polymer.2020.122283

[P104-2020] "Global polarization of Lambda and (Lambda) over-bar hyperons in Pb-Pb collisions at root s(NN)=2.76 and 5.02 TeV"

Acharya, S.; Adamova, D.; Adhya, S. P.; **Albuquerque, D. S. D.*; Chinellato, D. D.*; De Souza, R. D.*; Takahashi, J.***; et. al.; ALICE Collaboration

The global polarization of the Lambda and (Lambda) over bar hyperons is measured for Pb-Pb collisions at root s(NN) = 2.76 and 5.02 TeV recorded with the ALICE at the Large Hadron Collider (LHC). The results are reported differentially as a function of collision centrality and hyperon's transverse momentum (pT) for the range of centrality 5-50%, 0.5 < pT < 5 GeV/c, and rapidity vertical bar y vertical bar < 0.5. The hyperon global polarization averaged for Pb-Pb collisions at root s(NN) = 2.76 and 5.02 TeV is found to be consistent with zero, < P-H > (%) approximate to 0.01 +/- 0.06 (stat.) +/- 0.03 (syst.) in the collision centrality range 15-50%, where the largest signal is expected. The results are compatible with expectations based on an extrapolation from measurements at lower collision energies at the Relativistic Heavy Ion Collider, hydrodynamical model calculations, and empirical estimates based on collision energy dependence of directed flow, all of which predict the global polarization values at LHC energies of the order of 0.01%.

PHYSICAL REVIEW C 101[4], 044611, 2020. DOI: 10.1103/PhysRevC.101.044611

[P105-2020] "Graphene Supported MoS2 Structures with High Defect Density for an Efficient HER Electrocatalysts"

Joyner, J.; **Oliveira, E. F.***; Yamaguchi, H.; Kato, K.; Vinod, S.; **Galvao, D. S.***; Salpekar, D.; Roy, S.; Martinez, U.; Tiwary, C. S.; Ozden, S.; Ajayan, P. M.

The development of novel efficient and robust electrocatalysts with sufficient active sites is one of the key parameters for hydrogen evolution reactions (HER) catalysis, which plays a key role in hydrogen production for clean energy harvesting. Recently, two-dimensional (2D) materials, especially those based upon transition metal dichalcogenides such as molybdenum disulfide (MoS2), have gained attention for the catalysis of hydrogen production because of their exceptional properties. Innovative strategies have been developed to engineer these material systems for improvements in their catalytic activity. Toward this aim, the facile growth of MoS2 clusters by sulfurization of molybdenum dioxide (MoO2) particles supported on reduced graphene oxide (rGO) foams using the chemical vapor deposition (CVD) method is reported. This approach created various morphologies of MoS2 with large edges and defect densities on the basal plane of rGO supported MoS2 structures, which are considered as active sites for HER catalysis. In addition, MoS2 nanostructures on the surface of the porous rGO network show robust physical interactions, such as van der Waals and pi-pi interactions between MoS 2 and rGO. These features result in an improved process to yield a suitable HER catalyst. In order to gain a better understanding of the improvement of this MoS2-based HER catalyst, fully atomistic molecular dynamics (MD) simulations of different defect geometries were also performed.

ACS APPLIED MATERIALS & INTERFACES 12[11], 12629-12638, 2020. DOI: 10.1021/acsami.9b17713

[P106-2020] "HATS: A Ground-Based Telescope to Explore the THz Domain"

Castro, C. G. G. de; Raulin, J. P.; Valio, A.; **Marcon, R.***; et. al.

The almost unexplored frequency window from submillimeter to mid-infrared (mid-IR) may bring new clues about the particle acceleration and transport processes and the atmospheric thermal response during solar flares. Because of its technical complexity and the special atmospheric environment needed, observations at these frequencies are very sparse. The High Altitude THz Solar Photometer (HATS) is a full-Sun ground-based telescope designed to observe the continuum from the submillimeter to the mid-IR. It has a 457-mm spherical mirror with the sensor in its primary focus. The sensor is a Golay cell with high sensitivity in a very wide frequency range. The telescope has a polar mount, and a custom-built data acquisition system based on a 32 ksamples per second, 24 bits (72 dB dynamic range), 8 channels analog-to-digital board. Changing only the composition of the low- and band--pass filters in front of the Golay cell, the telescope can be setup to detect very different frequency bands; making the instrument very versatile. In this article we describe the telescope characteristics and its development status. Moreover, we give estimates of the expected fluxes during flares.

SOLAR PHYSICS 295[4], 56, 2020. DOI: 10.1007/s11207-020-01621-3

[P107-2020] "Influence of Magnetic Field on the Two-Photon Absorption and Hyper-Rayleigh Scattering of Manganese--Zinc Ferrite Nanoparticles"

Goncalves, E. S.; Cocca, L. H. Z.; Araujo, W. W. R.; Parekh, K.; Oliveira, C. L. P.; **Siqueira, J. P.*;** Mendonca, C. R.; De Boni, L.; Neto, A. M. F.

Magnetic nanoparticles based on manganese-zinc ferrite presenting spherical and cubic shapes, verified by small-angle X-rays scattering, were studied by means of the hyper-Rayleigh scattering, the Z-Scan technique in the open-aperture configuration, and a spectrally resolved femtosecond transient absorption setup.

Hyper-Rayleigh scattering and Z-Scan experiments were performed with applied magnetic field parallel to the laser polarization state and in the perpendicular direction. The hyperpolarizability of spherical nanoparticles was greater than the cubic ones due to the higher volume of spherical nanoparticles and, therefore, the increased influence of the spin-disoriented layer at the surface on cubic nanoparticles, resulting in a smaller orientational average contribution to the hyperpolarizability. The two-photon absorption cross section was the same for both samples, since the basic constituents are the same and the light absorption is not influenced by the surface anisotropy present on magnetic nanoparticles. For both nanoparticles, the measured optical second harmonic and the nonlinear absorption increased during experiments performed in the presence of external field in the parallel configuration, while a decrease was verified for experiments in the perpendicular case, which demonstrates a crystalline anisotropy on the nonlinear optical properties. Transient absorption measurements revealed an ultrafast relaxation process containing at least two separated dynamical processes, the faster with characteristic time below 1 ps and a longer one, much higher than 100 ps.

JOURNAL OF PHYSICAL CHEMISTRY C 124[12], 6784-6795, 2020. DOI: 10.1021/acs.jpcc.9b10208

[P108-2020] "Influence of the external pressure on the structure and magnetic properties of Nd0.5Sr0.5CoO3 cobaltite"

Torrao, R.; Caraballo Vivas, R. J.; Pimentel, B.; Santos, M. C.; **Paixao, L. S.***; dos Santos, A. M.; Reis, M. S.; Rocco, D. L.

The magnetic properties of the compound-type cobaltites LnACoO(3)(Ln = Lanthanide and A = alkaline-earth) are extremely dependent on the structural deformation, which can be induced by either chemical substitution or applying pressure. These two approaches are not equivalent because the atomic substitution changes the ratio of Co3+ and Co4+. It is well known that the additional electron of Co3+ plays a fundamental role in the magnetic and electric properties of these materials. Thus, the pressure is a way to influence the magnetic and electric properties considering only the structural deformation. In this work, pressure was applied to deform the structure of Nd0.5Sr0.5CoO3 and, thus, to elucidate its effect on the structural and magnetic properties. The findings show that even under pressure of 50 kbar, no structural phase transition was detected, but the unit cell volume significantly decreases by 2.8% and the Co-O-1-Co bond angle increases by 2.6%. However, the elasticity parameter (defined as the Co-O apical distance divided by the square root of the octahedral basal area) remained constant over the pressure range. The magnetic properties were evaluated up to 10.9 kbar, and the findings show that T-c varies with a rate of 0.5 K/kbar, and that the magnetic entropy change of the compound remains almost constant at a value of - 2 J/kg K for 5 T of magnetic field variation. The Co3+ and Co4+ ions were found to be in an intermediate spin state and remain the same over all studied pressure interval. To conclude, the structural deformation induced by the high pressure seem to not affect the magnetic properties, and the elasticity parameter is a useful tool sensitive to this change. These results indicate that, for strongly correlated electron system, the ratio of Co3+ and Co4+ is much more critical for changing the magnetic properties than the structural deformation.

JOURNAL OF MAGNETISM AND MAGNETIC MATERIALS 504 [166678], 2020 DOI: 10.1016/j.jmmm.2020.166678

[P109-2020] "Measurement of properties of B(s)(0)s -> mu(+) mu(-) decays and search for B-0 -> mu(+)mu(-) with the CMS experiment"

Sirunyan, A. M.; Tumasyan, A.; Adam, W.; **Chinellato, J. A.*; Tonelli Manganote, E. J.***; et. al.; CMS Collaboration

Results are reported for the B 0s ! + branching fraction and effective lifetime and from a search for the decay B0 ! + . The analysis uses a data sample of proton-proton collisions accumulated by the CMS experiment in 2011, 2012, and 2016, with center-of-mass energies (integrated luminosities) of 7TeV (5 fb), 8TeV (20 fb), and 13TeV (36 fb). The branching fractions are determined by measuring event yields relative to B+ ! J= K+ decays (with J= ! +), which results in the reduction of many of the systematic uncertainties. The decay B 0s ! + is observed with a significance of 5.6 standard deviations. The branching fraction is measured to be B (B 0s ! +) = [2:9 0:7(exp) 0:2(frag)] 10, where the first uncertainty combines the experimental statistical and systematic contributions, and the second is due to the uncertainty in the ratio of the B 0s and the B+ fragmentation functions. No significant excess is observed for the decay B0 ! + , and an upper limit of B(B0 ! +) < 3:6 10 is obtained at 95% confidence level. The B 0s ! + effective lifetime is measured to be + = 1:70 +0:61 ps. These results are consistent with standard model predictions.

JOURNAL OF HIGH ENERGY PHYSICS 4[188], 2020. DOI: 10.1007/JHEP04(2020)188

[P110-2020] "Measurement of strange baryon-antibaryon interactions with femtoscopic correlations"

Acharya, S.; Acosta, F. T.; Adam, J.; **Albuquerque, D. S. D.*; Chinellato, D. D.*; De Souza, R. D.*; Takahashi, J.***; et. al.; ALICE Collaboration

Two-particle correlation functions were measured for p (p) over bar, p (Lambda) over bar, (p) over bar Lambda, and Lambda(Lambda) over bar pairs in Pb-Pb collisions at root sNN = 2.76 TeV and root sNN = 5.02 TeV recorded by the ALICE detector. From a simultaneous fit to all obtained correlation functions, real and imaginary components of the scattering lengths, as well as the effective ranges, were extracted for combined p (Lambda) over bar and (p) over bar Lambda pairs and, for the first time, for Lambda(Lambda) over bar pairs. Effective averaged scattering parameters for heavier baryon--antibaryon pairs, not measured directly, are also provided. The results reveal similarly strong interaction between measured baryon-antibaryon pairs, suggesting that they all annihilate in the same manner at the same pair relative momentum k*. Moreover, the reported significant non-zero imaginary part and negative real part of the scattering length provide motivation for future baryon-antibaryon bound state searches.

PHYSICS LETTERS B 802[133223], 2020. DOI: 10.1016/j.physletb.2020.135223

[P111-2020] "Measurement of the t(t)over-barb(b)over-bar production cross section in the all-jet final state in pp collisions at root s=13 TeV"

Sirunyan, A. M.; Tumasyan, A.; Adam, W.; **Chinellato, J. A.*; Tonelli Manganote, E. J.***; et. al.; CMS Collaboration

A measurement of the production cross section of top quark pairs in association with two b jets (t (t) over barb (b) over bar) is presented using data collected in proton-proton collisions at root s=13 TeV by the CMS detector at the LHC corresponding to an integrated luminosity of 35.9 fb(-1). The cross section is measured in the all-jet decay channel of the top quark pair by selecting events containing at least eight jets, of which at least two are identified as originating from the hadronization of b quarks. A combination of multivariate analysis techniques is used to reduce the large background from multijet events not containing a top quark pair, and to help discriminate between jets originating from top quark decays and other additional jets.

The cross section is determined for the total phase space to be 5.5 +/- 0.3 (stat)(-1.3)(+)(1.6) (syst)pb and also measured for two fiducial t (t) over barb (b) over bar, definitions. The measured cross sections are found to be larger than theoretical predictions by a factor of 1.5-2.4, corresponding to 1-2 standard deviations.

PHYSICS LETTERS B 803[135285], 2020. DOI: 10.1016/j.physletb.2020.135285

[P112-2020] "Methodological differences can affect sequencing depth with a possible impact on the accuracy of genetic diagnosis"

Borges, M. G.*; Rocha, C. S.; Carvalho, B. S.; Lopes-Cendes, I.

For a better interpretation of variants, evidence-based databases, such as ClinVar, compile data on the presumed relationships between variants and phenotypes. In this study, we aimed to analyze the pattern of sequencing depth in variants from whole-exome sequencing data in the 1000 Genomes project phase 3, focusing on the variants present in the ClinVar database that were predicted to affect protein-coding regions. We demonstrate that the distribution of the sequencing depth varies across different sequencing centers (pair-wise comparison, p < 0.001). Most importantly, we found that the distribution pattern of sequencing depth is specific to each facility, making it possible to correctly assign 96.9% of the samples to their sequencing center. Thus, indicating the presence of a systematic bias, related to the methods used in the different facilities, which generates significant variations in breadth and depth in whole-exome sequencing data in clinically relevant regions. Our results show that methodological differences, leading to significant heterogeneity in sequencing depth, may potentially influence the accuracy of genetic diagnosis. Furthermore, our findings highlight how it is still challenging to integrate results from different sequencing centers, which may also have an impact on genomic research.

GENETICS AND MOLECULAR BIOLOGY 43[2], UNSP e20190270, 2020. DOI: 10.1590/1678-4685-GMB-2019-0270

[P113-2020] "Microfluidic Mixer with Automated Electrode Switching for Sensing Applications"

Braunger, M. L.*; Fier, I.; **Rodrigues, V.*;** Arratia, P. E.; **Riul Junior, A.***

An electronic tongue (e-tongue) is a multisensory system usually applied to complex liquid media that uses computational/statistical tools to group information generated by sensing units into recognition patterns, which allow the identification/distinction of samples. Different types of e-tongues have been previously reported, including microfluidic devices. In this context, the integration of passive mixers inside microchannels is of great interest for the study of suppression/enhancement of sensorial/chemical effects in the pharmaceutical, food, and beverage industries. In this study, we present developments using a stereolithography technique to fabricate microfluidic devices using 3D-printed molds for elastomers exploring the staggered herringbone passive mixer geometry. The fabricated devices (microchannels plus mixer) are then integrated into an e-tongue system composed of four sensing units assembled on a single printed circuit board (PCB). Gold-plated electrodes are designed as an integral part of the PCB electronic circuitry for a highly automated platform by enabling faster analysis and increasing the potential for future use in commercial applications. Following previous work, the e-tongue sensing units are built functionalizing gold electrodes with layer-by-layer (LbL) films. Our results show that the system is capable of (i) covering basic tastes below the human gustative perception and (ii) distinguishing different suppression effects coming from the mixture of both strong and weak electrolytes. This setup allows for triplicate measurements in 12 electrodes, which represents four complete sensing units, by automatically switching all electrodes without any physical interaction with the sensor. The result is a fast and reliable data acquisition system, which comprises a suitable solution for monitoring, sequential measurements, and database formation, being less susceptible to human errors.

CHEMOSENSORS 8[1][13], 2020. DOI: 10.3390/chemosensors8010013

[P114-2020] "Mid-Infrared Frequency Comb Generation and Spectroscopy with Few-Cycle Pulses and chi((2)) Nonlinear Optics"

Lind, A. J.; Kowligy, A.; Timmers, H.; **Cruz, F. C.***; Nader, N.; Silfies, M. C.; Allison, T. K.; Diddams, S. A.

The mid-infrared atmospheric window of 3-5.5 mu m holds valuable information regarding molecular composition and function for fundamental and applied spectroscopy. Using a robust, mode-locked fiberlaser source of < U fs pulses in the near infrared, we explore quadratic (chi((2))) nonlinear optical processes leading to frequency comb generation across this entire mid-infrared atmospheric window. With experiments and modeling, we demonstrate intrapulse difference frequency generation that yields few-cycle mid-infrared pulses in a single pass through periodically poled lithium niobate. Harmonic and cascaded chi((2)) nonlinearities further provide direct access to the carrier-envelope offset frequency of the near infrared driving pulse train. The high frequency stability of the mid-infrared frequency comb is exploited for spectroscopy of acetone and carbonyl sulfide with simultaneous bandwidths exceeding 11 THz and with spectral resolution as high as 0.003 cm(-1). The combination of low noise and broad spectral coverage enables detection of trace gases with concentrations in the part-per-billion range.

PHYSICAL REVIEW LETTERS 124[13], 133904, 2020. DOI: 10.1103/PhysRevLett.124.133904

[P115-2020] "Observation of the Lambda(0)(b) -> J/psi Lambda phi decay in proton-proton collisions at root s=13 TeV"

Sirunyan, A. M.; Tumasyan, A.; Adam, W.; **Chinellato, J. A.*; Tonelli Manganote, E. J.***; et. al.; CMS Collaboration

The observation of the Lambda(0)(b) -> J/psi Lambda phi decay is reported using proton-proton collision data collected at root s = 13TeV by the CMS experiment at the LHC in 2018, corresponding to an integrated luminosity of 60fb(-1). The ratio of the branching fractions B(Lambda(0)(b) -> J/psi Lambda phi)/B(Lambda(0)(b) > psi(2S)Lambda) is measured to be (8.26 +/- 0.90 (stat) +/- 0.68 (syst) +/- 0.11 (B)) x 10(-2), where the first uncertainty is statistical, the second is systematic, and the last uncertainty reflects the uncertainties in the world-average branching fractions of phi and psi(2S) decays to the reconstructed final states.

PHYSICS LETTERS B 802[135203], 2020. DOI: 10.1016/j.physletb.2020.135203

[P116-2020] "On the (in)efficacy of motor imagery training without feedback and event-related desynchronizations considerations"

Stefano Filho, C. A.*; Costa, T. B. S.; Uribe, L. F.; Rodrigues, P. G.; Soriano, D. C.; Attux, R.; **Castellano, G.***

Motor imagery (MI) constitutes a recurrent strategy for signals generation in brain-computer interfaces (BCIs) - systems that aim to control external devices by directly associating brain responses to distinct commands. Although great improvement has been achieved in MI-BCIs performance over recent years, they still suffer from inter- and intra-subject variability issues. As an attempt to cope with this, some studies have suggested that MI training should aid users to appropriately modulate their response for BCI usage: generally, this training is performed based on the sensorimotor rhythms' modulation over the primary sensorimotor cortex (PMC), with the signal being feedbacked to the user. Nonetheless, recent studies have revisited the actual involvement of the PMC into MI, and little to no attention has been devoted to understanding the participation of other cortical areas into training protocols. Therefore, in this work, our aim was to analyze the response induced by hands MI of 10 healthy subjects in the form of event-related desynchronizations (ERDs) and to assess whether features from beyond the PMC might be useful for hands MI classification. We investigated how this response occurs for distinct frequency intervals between 7-30 Hz, and ex0plored changes in their evocation pattern across 12 MI training sessions without feedback. Overall, we found that ERD patterns occur differently for the frequencies encompassed by the mu and beta bands, with its evocation being favored for the first band. Over time, the no-feedback approach was inefficient to aid in enhancing ERD evocation (EO). Moreover, to some extent, EO tends to decrease over blocks within a given run, and runs within an MI session, but remains stable within an MI block. We also found that the C3/C4 pair is not necessarily optimal for data classification, and both spectral and spatial subjects' specificities should be considered when designing training protocols.

BIOMEDICAL PHYSICS & ENGINEERING EXPRESS 6[3], 035030, 2020. DOI: 10.1088/2057-1976/ab8992

[P117-2020] "Optimizing automatic morphological classification of galaxies with machine learning and deep learning using Dark Energy Survey imaging"

Cheng, T. Y.; Conselice, C. J.; Aragon-Salamanca, A.; **Sobreira, F.***; et. al.

There are several supervised machine learning methods used for the application of automated morphological classification of galaxies; however, there has not yet been a clear comparison of these different methods using imaging data, or an investigation for maximizing their effectiveness. We carry out a comparison between several common machine learning methods for galaxy classification [Convolutional Neural Network (CNN), K-nearest neighbour, logistic regression, Support Vector Machine, Random Forest, and Neural Networks] by using Dark Energy Survey (DES) data combined with visual classifications from the Galaxy Zoo 1 project (GZ1). Our goal is to determine the optimal machine learning methods when using imaging data for galaxy classification. We show that CNN is the most successful method of these ten methods in our study. Using a sample of similar to 2800 galaxies with visual classification from GZ1, we reach an accuracy of similar to 0.99 for the morphological classification of ellipticals and spirals. The further investigation of the galaxies that have a different ML and visual classification but with high predicted probabilities in our CNN usually reveals the incorrect classification provided by GZ1. We further find the galaxies having a low probability of being either spirals or ellipticals are visually lenticulars (S0), demonstrating that supervised learning is able to rediscover that this class of galaxy is distinct from both ellipticals and spirals. We confirm that similar to 2.5 per cent galaxies are misclassified by GZ1 in our study. After correcting these galaxies' labels, we improve our CNN performance to an average accuracy of over 0.99 (accuracy of 0.994 is our best result).

MONTHLY NOTICES OF THE ROYAL ASTRONOMICAL SOCIETY 493[3], 4209-4228, 2020. DOI: 10.1093/mnras/staa501

[P118-2020] "Orbitally defined field-induced electronic state in a Kondo lattice"

Lesseux, G. G.*; Sakai, H.; Hattori, T.; Tokunaga, Y.; Kambe, S.; Kuhns, P. L.; Reyes, A. P.; Thompson, J. D.; **Pagliuso, P. G.*; Urbano, R. R.***

CeRhIn5 is a Kondo-lattice prototype in which a magnetic field B* similar or equal to 31 T induces an abrupt Fermi-surface (FS) reconstruction and pronounced in-plane electrical transport anisotropy all within its antiferromagnetic state. Though the antiferromagnetic order at zero field is well understood, the origin of an emergent state at B* remains unknown due to challenges inherent to probing states microscopically at high fields. Here we report low-temperature nuclear magnetic resonance (NMR) measurements revealing a pronounced decrease in the In-115 formal Knight shift, without changes in crystal or magnetic structures, of CeRhIn5 at fields (parallel to c) spanning B*. We discuss the emergent state above B* in terms of a change in Ce's 4f orbitals that arises from field-induced evolution of crystal-electric field (CEF) energy levels. This change in orbital character enhances hybridization between the 4f and the conduction electrons that leads ultimately to an itinerant quantum-critical point at B-c0 similar or equal to 50 T.

PHYSICAL REVIEW B 101[16], 165111, 2020. DOI: 10.1103/PhysRevB.101.165111

[P119-2020] "Performance of the reconstruction and identification of high-momentum muons in proton-proton collisions at root s=13 TeV"

Sirunyan, A. M.; Tumasyan, A.; Adam, W.; **Chinellato, J. A.*; Tonelli Manganote, E. J.***; et. al.; CMS Collaboration

The CMS detector at the LHC has recorded events from proton-proton collisions, with muon momenta reaching up to 1.8 TeV in the collected dimuon samples. These high-momentum muons allow direct access to new regimes in physics beyond the standard model. Because the physics and reconstruction of these muons are different from those of their lower-momentum counterparts, this paper presents for the first time dedicated studies of efficiencies, momentum assignment, resolution, scale, and showering of very high momentum muons produced at the LHC. These studies are performed using the 2016 and 2017 data sets of proton-proton collisions at root s = 13 TeV with integrated luminosities of 36.3 and 42.1 fb(-1), respectively.

JOURNAL OF INSTRUMENTATION 15[2], P02027, 2020. DOI: 10.1088/1748-0221/15/02/P02027

[P120-2020] "Polyfuran-based chemical sensors: reactivity analysis via Fukui indexes and reactive molecular dynamics"

Lascane, L. G.; **Oliveira, E. F.***; Batagin Neto, A.

In the present study we employ electronic structure calculations (based on Density Functional Theory -DFT approach) and Fully Atomistic Reactive Molecular Dynamics (FARMD) simulations (based on ReaxFF reactive force field) to evaluate the reactivity of branched polyfuran (PF) derivatives and identify promising systems for chemical sensing. Condensed-to-atoms Fukui indexes (CAFI) were employed to identify the most reactive sites on the oligomers structure. The chemical sensing abilities of the most promising systems were evaluated via FARMD simulations in the presence of distinct gaseous compounds. The results indicate the derivatives PF-CCH and PF--NO & x2082; (i.e. CCH and NO2 as side groups) as the most promising systems for chemical sensor applications, presenting higher reactivity on the most accessible sites. An interesting correspondence between DFT and MD results was also identified, suggesting the plausibility of using CAFI parameters for the identification of improved materials for chemical sensors.

MRS ADVANCES 5[10][SI], 497-503, 2020. DOI: 10.1557/adv.2020.203

[P121-2020] "Possible quantum fluctuations in the vicinity of the quantum critical point of (Sr, Ca)(3)Ir4Sn13 revealed by high-energy x-ray diffraction"

Veiga, L. S., I; Mardegan, J. R. L.; Zimmermann, M., V; **Maimone, D. T.***; Carneiro, F. B.; Fontes, M. B.; Strempfer, J.; **Granado, E.*; Pagliuso, P. G.***; Bittar, E. M.

We explore the evolution of the structural phase transition of (Sr, Ca)(3)Ir4Sn13, a model system to study the interplay between structural quantum criticality and superconductivity, by means of high-energy x-ray diffraction measurements at high pressures and low temperatures. Our results confirm a rapid suppression of the superlattice transition temperature T* against pressure, which extrapolates to zero at a critical pressure of approximate to 1.79(4) GPa. The temperature evolution of the superlattice Bragg peak in Ca3Ir4Sn13 reveals a drastic decrease of the intensity and an increase of the linewidth when T -> 0 K and p -> p(c). Such anomaly is likely associated with the emergence of quantum fluctuations that disrupt the formation of long-range superlattice modulation. The revisited temperature-pressure phase diagram of (Sr, Ca)(3)Ir4Sn13 thus highlights the intertwined nature of the distinct order parameters present in this system and demonstrates some similarities between this family and the unconventional superconductors.

PHYSICAL REVIEW B 101[10], 104511, 2020. DOI: 10.1103/PhysRevB.101.104511

[P122-2020] "Probing Surface Effects on alpha-NaYF4 Nanoparticles by Nuclear Magnetic Resonance"

Queiroz, T. B. de; Cabrera-Baez, M.; **Menegasso, P.***; Martinez, E. D.; **Garcia Flores, A. F.*; Rettori, C.*; Urbano, R. R.***

The structural properties of insulating alpha-NaYF4 (cubic) nanopartides with size ranging within 4-25 nm were investigated by high-resolution Na-23 and F-19 solid-state nuclear magnetic resonance (NMR) spectroscopy under magic an spinning (MAS) with single-pulse (SP-MAS), spin-echo (SEMAS), inversion recovery, and 3QMAS experiments. The Na-23 SP-MAS spectra show a broad peak around -18 ppm with a shoulder around -9 ppm, which becomes more prominent for the smallest nanoparticles. The Na-23 nuclei resonating around -9 ppm demonstrate a longitudinal relaxation time of a few milliseconds, while the ones resonating around -18 ppm are on the order of 50-125 ms. This feature is noticed for all studied nanopartides, but it is more evident for the smallest ones (phi less than or similar to 7 nm), especially among the batches with higher polydispersity. On the basis of these relaxation times, field-dependent measurements, and Na-23 3QMAS, we attributed the signal around -18 ppm to Na-23 in the bulk of the nanopartides and the signal around -9 ppm to surface or/and sites near defects, featuring higher fluctuations in the electric field gradient (EFG). The Na-23 3QMAS spectra provide evidence for two (and sometimes three) distinct Na sites in alpha-NaYF4 with similar quadrupole coupling but slightly different chemical shifts. The F-19 SE-MAS spectra show a broad peak around -75 ppm with a small shoulder around -120 ppm corresponding to only 1% of the signal. The peak around -75 ppm is attributed to the stoichiometric NaYF4 composition, and its broadening is attributed to a distribution of Na- and Y-rich environments. The minor shoulder around -120 ppm is associated with the F-deficient NaYF4 structure. The F-19 spin-spin relaxation time indicates some degree of mobility of the fluorine atoms, possibly due to the presence of F vacancies triggering hopping-like ion motion. The signal related to the F-deficient structure is greatly enhanced for the smallest nanoparticles (phi = 4 nm), i.e., along with the increase of 23 Na surface effects and defects. Therefore, we correlate several NMR techniques to provide a fundamental structural view for nanopartides used as upconversion host systems with prominent technological applications. Particularly for alpha-NaYF4, significant surface effects and defects must be expected for nanoparticles with dimensions in the order of few nanometers (phi less than or similar to 7 nm).

JOURNAL OF PHYSICAL CHEMISTRY C 124[17], 9523-9535, 2020. DOI: 10.1021/acs.jpcc.0c00776

[P123-2020] "Production and characterization of promising beta-stable seed crystals to modulate the crystallization of fat-based industrial products"

Santos, C. A. dos; Carpenter, C. S.; Arid, J. D.; Silva, A. A. da; **Cardoso, L. P.***; Ribeiro, A. P. B.; Efraim, P.

Spray cooling or spray chilling is a technique for obtaining solid lipid microparticles (SLMs) within the diameter range in micrometers using low temperatures and no organic solvents. It is a low-cost technique and is easy to scale-up. The production of SLMs into beta-form represents a technological challenge due to the fast crystallization given by the spray cooling system, which generally results in SLMs crystallized into the metastable polymorphic form a. This study focuses on the production and characterization of SLMs by spray cooling using hard fat soybean oil (HS) added of D-limonene or canola oil, aiming to their application as beta-seed crystals into lipid systems. The beta--seed crystals could turn into an alternative lipid material to be used in fat-based products that present the preferential beta' crystallization, like palm oil, increasing its compatibility with cocoa butter (CB) and allowing for the development of substitutes. The obtained SLMs showed spherical geometry and no agglomeration during storage at 25 degrees C for up to 30 days, verified by scanning electron microscopy (SEM). The mean diameters (D-50) were between 150 and 200 pm and the beta' and beta-form, determined by X-ray diffraction (XRD), appeared immediately after the crystallization process by spray cooling using HS added of 5% D-limonene (the HS control sample presented only the alpha-form). The SLMs of this study demonstrated their potential use as beta-seed crystals into lipid systems.

FOOD RESEARCH INTERNATIONAL 130[108900], 2020. DOI: 10.1016/j.foodres.2019.108900

[P124-2020] "Production of (anti-)He-3 and (anti-)H-3 in p-Pb collisions at root s(NN)=5.02 TeV"

Acharya, S. Adamova, D.; Adler, A.; **Albuquerque, D. S. D.*; Chinellato, D. D.*; Takahashi, J.***; et. al.; ALICE Collaboration

The transverse momentum (p(T)) differential yields of (anti-)He-3 and (anti-)H-3 measured in p-Pb collisions at root s(NN) = 5.02 TeV with ALICE at the Large Hadron Collider (LHC) are presented. The ratios of the p(T)-integrated yields of (anti-)He-3 and (anti-)H-3 to the proton yields are reported, as well as the pT dependence of the coalescence parameters B-3 for (anti-)He-3 and (anti-)H-3. For (anti-)He-3, the results obtained in four classes of the mean charged--particle multiplicity density are also discussed. These results are compared to predictions from a canonical statistical hadronization model and coalescence approaches. An upper limit on the total yield of (4)(He) over bar is determined.

PHYSICAL REVIEW C 101[4], 044906, 2020. DOI: 10.1103/PhysRevC.101.044906

[P125-2020] "Production of charged pions, kaons, and (anti-)protons in Pb-Pb and inelastic pp collisions at root s(NN)=5.02 TeV"

Acharya, S.; Adamova, D.; Adhya, S. P.; **Albuquerque, D. S. D.*; Chinellato, D. D.*; De Souza, R. D.*; Takahashi, J.*;** et. al.; ALICE Collaboration

Midrapidity production of pi(+/-), K-+/-, and (<(p))over bar>p measured by the ALICE experiment at the CERN Large Hadron Collider, in Pb-Pb and inelastic pp collisions at root s(NN) = 5.02 TeV, is presented. The invariant yields are measured over a wide transverse momentum (p(T)) range from hundreds of MeV/c up to 20 GeV/c. The results in Pb-Pb collisions are presented as a function of the collision centrality, in the range 0-90%. The comparison of the P-T -integrated particle ratios, i.e., proton-to-pion (p/pi) and kaon-to-pion (K/pi) ratios, with similar measurements in Pb-Pb collisions at root s(NN) = 2.76 TeV show no significant energy dependence. Blast-wave fits of the p(T) spectra indicate that in the most central collisions radial flow is slightly larger at 5.02 TeV with respect to 2.76 TeV. Particle ratios (p/pi, K/pi) as a function of p(T) show pronounced maxima at p(T) approximate to 3 GeV/c in central Pb-Pb collisions. At high p(T) , particle ratios at 5.02 TeV are similar to those measured in pp collisions at the same energy and in Pb-Pb collisions at root sNN = 2.76 TeV. Using the pp reference spectra measured at the same collision energy of 5.02 TeV, the nuclear modification factors for the different particle species are derived. Within uncertainties, the nuclear modification factor is particle species independent for high p(T) and compatible with measurements at root sNN = 2.76 TeV. The results are compared to state-of-the-art model calculations, which are found to describe the observed trends satisfactorily.

PHYSICAL REVIEW C 101[4], 044907, 2020. DOI: 10.1103/PhysRevC.101.044907

[P126-2020] "Production of Lambda(+)(c) baryons in proton--proton and lead-lead collisions at root S-NN=5.02 TeV"

Sirunyan, A. M.; Tumasyan, A.; Adam, W.; **Chinellato, J. A.*; Tonelli Manganote, E. J.*;** et. al.; CMS Collaboration

The transverse momentum (P-T) spectra of inclusively produced A c P baryons are measured via the exclusive decay channel Lambda(+)(c) -> pK(-)pi(+) using the CMS detector at the LHC. Spectra are measured as a function of transverse momentum in proton-proton (pp) and lead-lead (PbPb) collisions at a nucleonnucleon center-of-mass energy of 5.02TeV. The measurement is performed within the Lambda(+)(c) rapidity interval vertical bar Y vertical bar < 1 in the p(T) range of 5-20GeV/c in pp and 10-20GeV/c in PbPb collisions. The observed yields of Lambda(+)(c) for p(T) of 10-20 GeV/c suggest a suppression in central PbPb collisions compared to pp collisions scaled by the number of nucleon-nucleon (NN) interactions. The Lambda(+)(c)/D-0 production ratio in pp collisions is compared to theoretical models. In PbPb collisions, this ratio is consistent with the result from pp collisions in their common p-r range.

PHYSICS LETTERS B 803[135328], 2020. DOI: 10.1016/j.physletb.2020.135328

[P127-2020] "Revealing the Role of Tin(IV) Halides in the Anisotropic Growth of CsPbX3 Perovskite Nanoplates"

Bonato, L. G.*; Moral, R. F.; **Nagamine, G.*; Alo, A.*;** Germino, J. C.; Silva, D. S. da; **Almeida, D. B.*; Zagonel, L. F.*;** Galembeck, F.; **Padilha, L. A.***; Nogueira, A. F.

CsPbX3 perovskite nanoplates (PNPLs) were formed in a synthesis driven by SnX4 (X=Cl, Br, I) salts. The role played by these hard Lewis acids in directing PNPL formation is addressed. Sn4+ disturbs the acid-base equilibrium of the system, increasing the protonation rate of oleylamine and inducing anisotropic growth of nanocrystals. Sn4+ cations influence the reaction dynamics owing to complexation with oleylamine molecules. By monitoring the photoluminescence excitation and photoluminescence (PL) spectra of the PNPLs grown at different temperatures, the influence of the thickness on their optical properties is mapped. Time-resolved and spectrally resolved PL for colloidal dispersions with different optical densities reveals that the dependence of the overall PL lifetime on the emission wavelength do not originate from energy transfer between PNPLs but from the contribution of PNPLs with distinct thickness, indicating that thicker PNPLs exhibit longer PL lifetimes.

ANGEWANDTE CHEMIE-INTERNATIONAL EDITION, 2020. DOI: 10.1002/anie.202002641

[P128-2020] "Running of the top quark mass from proton--proton collisions at root s=13 TeV"

Sirunyan, A. M.; Tumasyan, A.; Adam, W.; **Chinellato, J. A.*; Tonelli Manganote, E. J.***; et. al.; CMS Collaboration

The running of the top quark mass is experimentally investigated for the first time. The mass of the top quark in the modified minimal subtraction ((MS) over bar) renormalization scheme is extracted from a comparison of the differential top quark-antiquark (t (t) over bar) cross section as a function of the invariant mass of the t (t) over bar system to next-to-leading-order theoretical predictions. The differential cross section is determined at the parton level by means of a maximum--likelihood fit to distributions of final-state observables. The analysis is performed using t (t) over bar candidate events in the e(+/-)mu(-/+) channel in proton-proton collision data at a centre-of-mass energy of 13 TeV recorded by the CMS detector at the CERN LHC in 2016, corresponding to an integrated luminosity of 35.9 fb(-1). The extracted running is found to be compatible with the scale dependence predicted by the corresponding renormalization group equation. In this analysis, the running is probed up to a scale of the order of 1 TeV.

PHYSICS LETTERS B 803[135263], 2020. DOI: 10.1016/j.physletb.2020.135263

[P129-2020] "Search for a Narrow Resonance Lighter than 200 GeV Decaying to a Pair of Muons in Proton-Proton Collisions at root s=13 TeV"

Sirunyan, A. M.; Tumasyan, A.; Adam, W.; **Chinellato, J. A.*; Tonelli Manganote, E. J.***; et. al.; CMS Collaboration

A search is presented for a narrow resonance decaying to a pair of oppositely charged muons using root s = 13 TeV proton-proton collision data recorded at the LHC. In the 45-75 and 110-200 GeV resonance mass ranges, the search is based on conventional triggering and event reconstruction techniques. In the 11.5-45 GeV mass range, the search uses data collected with dimuon triggers with low transverse momentum thresholds, recorded at high rate by storing a reduced amount of trigger-level information. The data correspond to integrated luminosities of 137 and 96.6 fb(-1) for conventional and high-rate triggering, respectively. No significant resonant peaks are observed in the probed mass ranges. The search sets the most stringent constraints to date on a dark photon in the similar to 30-75 and 110-200 GeV mass ranges.

PHYSICAL REVIEW LETTERS 124[13], 131802, 2020. DOI: 10.1103/PhysRevLett.124.131802

[P130-2020] "Search for direct pair production of supersymmetric partners to the tau lepton in proton-proton collisions at root s=13TeV"

Sirunyan, A. M.; Tumasyan, A.; Adam, W.; **Chinellato, J. A.*; Tonelli Manganote, E. J.*;** et. al.; CMS Collaboration

A search is presented for t slepton pairs produced in proton--proton collisions at a center-of-mass energy of 13 TeV. The search is carried out in events containing two t leptons in the final state, on the assumption that each t slepton decays primarily to a t lepton and a neutralino. Events are considered in which each t lepton decays to one or more hadrons and a neutrino, or in which one of the t leptons decays instead to an electron or a muon and two neutrinos. The data, collected with the CMS detector in 2016 and 2017, correspond to an integrated luminosity of 77.2 fb-1. The observed data are consistent with the standard model background expectation. The results are used to set 95% confidence level upper limits on the cross section for t slepton pair production in various models for t slepton masses between 90 and 200 GeV and neutralino masses of 1, 10, and 20 GeV. In the case of purely left-handed t slepton production and decay to a t lepton and a neutralino with a mass of 1GeV, the strongest limit is obtained for a t slepton mass of 125 GeV at a factor of 1.14 larger than the theoretical cross section.

EUROPEAN PHYSICAL JOURNAL C 80 [3], 189, 2020. DOI: 10.1140/epjc/s10052-020-7739-7

[P131-2020] "Search for heavy Higgs bosons decaying to a top quark pair in proton-proton collisions at root s = 13 TeV"

Sirunyan, A. M.; Tumasyan, A.; Adam, W.; **Chinellato, J. A.*; Tonelli Manganote, E. J.*;** et. al.; CMS Collaboration

A search is presented for additional scalar (H) or pseudoscalar (A) Higgs bosons decaying to a top quark pair in proton-proton collisions at a center-of-mass energy of 13 TeV. The data set analyzed corresponds to an integrated luminosity of 35.9 fb(-1) collected by the CMS experiment at the LHC. Final states with one or two charged leptons are considered. The invariant mass of the reconstructed top quark pair system and variables that are sensitive to the spin of the particles decaying into the top quark pair are used to search for signatures of the H or A bosons. The interference with the standard model top quark pair background is taken into account. A moderate signal-like deviation compatible with an A boson with a mass of 400 GeV is observed with a global significance of 1.9 standard deviations. New stringent constraints are reported on the strength of the coupling of the hypothetical bosons to the top quark, with the mass of the bosons ranging from 400 to 750 GeV and their total relative width from 0.5 to 25%. The results of the search are also interpreted in a minimal supersymmetric standard model scenario. Values of m(A) from 400 to 700 GeV are probed, and a region with values of tan beta below 1.0 to 1.5, depending on m(A), is excluded at 95% confidence level.

JOURNAL OF HIGH ENERGY PHYSICS 4[171], 2020. DOI: 10.1007/JHEP04(2020)171

[P132-2020] "Search for supersymmetry in pp collisions at root s=13 TeV with 137 fb(-1) in final states with a single lepton using the sum of masses of large-radius jets"

Sirunyan, A. M.; Tumasyan, A.; Adam, W.; **Chinellato, J. A.*; Tonelli Manganote, E. J.***; et. al.; CMS Collaboration

Results are reported from a search for new physics beyond the standard model in proton-proton collisions in final states with a single lepton; multiple jets, including at least one jet tagged as originating from the hadronization of a bottom quark; and large missing transverse momentum. The search uses a sample of proton-proton collision data at root s =13 TeV, corresponding to 137 fb(-1), recorded by the CMS experiment at the LHC. The signal region is divided into categories characterized by the total number of jets, the number of bottom quark jets, the missing transverse momentum, and the sum of masses of large-radius jets. The observed event yields in the signal regions are consistent with estimates of standard model backgrounds based on event yields in the control regions. The results are interpreted in the context of simplified models of supersymmetry involving gluino pair production in which each gluino decays into a top quark--antiquark pair and a stable, unobserved neutralino, which generates missing transverse momentum in the event. Scenarios with gluino masses up to about 2150 GeV are excluded at 95% confidence level (or more) for neutralino masses up to 700 GeV. The highest excluded neutralino mass is about 1250 GeV, which holds for gluino masses around 1850 GeV.

PHYSICAL REVIEW D 101[5], 052010, 2020. DOI: 10.1103/PhysRevD.101.052010

[P133-2020] "Solar neutrino limits on decoherence"

Holanda, P. C. de*

The solar neutrino flux arrives at Earth as an incoherent admixture of mass eigenstates, and then solar neutrino detection constitute a blind probe to the oscillation pattern of the neutrino flavour conversion. Consequently, it is also impossible to probe, in a model independent approach, any new physics that leads to an enhancement of decoherence during the neutrino evolution, an effect that is present for instance in Open Quantum System formalism. However, such mechanism can also induce changes between mass eigenstates if an energy interchange between the neutrino subsystem and the reservoir is not explicitly forbiden. In this work the conversion probabilities between mass eigenstates in an Open Quantum System are calculated, and limits are stablished for these kind of transitions. We present our results in a pedagogical way, pointing out how far the analysis can go without any assumption on the neutrino conversion physics inside the Sun, before performing the full calculations. We obtain as limits for the decoherence parameters the values of Gamma(3) < 6.5 x 10(-19) eV and Gamma(8) < 7.1 x 10(-19) eV at 3 sigma.

JOURNAL OF COSMOLOGY AND ASTROPARTICLE PHYSICS 3[012], 2020. DOI: 10.1088/1475-7516/2020/03/012

[P134-2020] "Strain-controlled ferromagnetism in BiFeO3 nanoparticles"

Ramos, E.; Cardona-Rodriguez, A.; Carranza-Celis, D.; Gonzalez-Hernandez, R.; **Muraca, D.***; Gabriel Ramirez, J.

Multiferroic materials are at the core of voltage-controlled spintronic devices. Therefore, an understanding of the underlying electronic correlations and their effects associated with their complex energy landscape is an important and ongoing task. One key parameter in oxide-based perovskite multiferroics is their sensitivity to strain effects under confinement. Here, we report on the ferromagnetism induced by strain-engineering at the nanoscale on BiFeO3 (BFO) nanoparticles. By controlling synthesis parameters, we were able to modify the BFO lattice parameters up to 0.15% and as a consequence, induce ferromagnetism in otherwise antiferromagnetic bulk BFO. In order to understand the driving mechanisms behind such an effect, we performed density functional theory calculations (DFT) using the BFO parameters obtained from the experiment. We found that small distortions of the structural lattice parameters of the order of 0.01% are sufficient to induce a significant spin imbalance close to the Fermi energy at the Fe sites.

This may explain the appearance of weak ferromagnetism in strained BFO thin films reported earlier and offers a new route to novel voltage-controlled spintronic devices based on multiferroic materials.

JOURNAL OF PHYSICS-CONDENSED MATTER 32[18], 185703, 2020. DOI: 10.1088/1361-648X/ab6b8a

[P135-2020] "Study of excited Lambda(0)(b) states decaying to Lambda(0)(b)pi(+)pi(-) in proton-proton collisions at root s=13TeV"

Sirunyan, A. M.; Tumasyan, A.; Adam, W.; **Chinellato, J. A.*; Tonelli Manganote, E. J.***; et. al.; CMS Collaboration

A study of excited Lambda(0)(b) baryons is reported, based on a data sample collected in 2016-2018 with the CMS detector at the LHC in proton-proton collisions at a center-of-mass energy of 13 TeV, corresponding to an integrated luminosity of up to 140fb(-1). The existence of four excited Lambda(0)(b) states: Lambda(0)(b) (5912)(0), Lambda(0)(b) (5920)(0), Lambda(0)(b) (6146)(0), and Lambda(0)(b) (6152)(0) in the Lambda(0)(b)pi(+)pi(-) mass spectrum is confirmed, and their masses are measured. The Lambda(0)(b)pi(+)pi(-) mass distribution exhibits a broad excess of events in the region of 6040-6100 MeV, whose origin cannot be discerned with the present data.

PHYSICS LETTERS B 803[135345], 2020. DOI: 10.1016/j.physletb.2020.135345

[P136-2020] "Sympatric speciation based on pure assortative mating"

Caetano, R. A.; Sanchez, S.; Costa, C. L. N.; **Aguiar, M. A. M. de***

Although geographic isolation has been shown to play a key role in promoting reproductive isolation, it is now believed that speciation can also happen in sympatry and with considerable gene flow. Here we present a model of sympatric speciation based on assortative mating that does not require a genetic threshold for reproduction, i.e., that does not directly associate genetic differences between individuals with reproductive incompatibilities. In the model individuals mate with the most similar partner in their pool of potential mates, irrespective of how dissimilar it might be. We show that assortativity alone can lead to the formation of clusters of genetically similar individuals. The absence of a minimal genetic similarity for mating implies the constant generation of hybrids and brings up the old problem of species definition. Here, we define species based on clustering of genetically similar individuals but allowing genetic flow among different species. We show that the results obtained with the present model are in good agreement with empirical data, in which different species can still reproduce and generate hybrids.

JOURNAL OF PHYSICS A-MATHEMATICAL AND THEORETICAL 53[15], 155601, 2020. DOI: 10.1088/1751-8121/ab7b9f

[P137-2020] "Synthesis and magnetic interaction on concentrated Fe3O4 nanoparticles obtained by the co-precipitation and hydrothermal chemical methods"

Jesus, A. C. B.; Jesus, J. R.; Lima, R. J. S.; **Moura, K. O.*;** Almeida, J. M. A.; Duque, J. G. S.; Meneses, C. T.

In this work, a comparative study of the synthesis and magnetic properties of Fe3O4 nanoparticles obtained by the co-precipitation and hydrothermal methods with the adding of the sucrose as a chelating agent is reported. The analysis of transmission electron microscopy (TEM) show that particles are spherical-like with an average particle size ranging of 3 <= d <= 10 nm. Magnetization measurements as a function of an applied magnetic field and temperature are consistent with a superparamagnetic behavior with small T-B values. The analysis of the MvsH loops measured at T = 2 K and Zero-Field-Cooled and Field-Cooled (ZFC - FC) curves allows us to estimate the average diameter of Fe3O4 nanoparticles. These results are in good agreement with those obtained through X-ray diffraction (XRD) data (by using Scherrer equation and Williamson-Hall plot) and slightly smaller than those estimated using TEM images. Finally, ZFC - FC data are also used to evaluate the effective anisotropy constants, which are similar to those values found in literature considering the average sizes values estimated by different techniques.

CERAMICS INTERNATIONAL 46 [8A], 11149-11153, 2020. DOI: 10.1016/j.ceramint.2020.01.135

[P138-2020] "The ideal hydrodynamic limit and non-Abelian gauge symmetries"

Torrieri, G.*

We show that the ideal fluid local equilibrium limit, defined as the existence of a flow frame u mu which characterises the direction of both a conserved entropy current and conserved charge currents is incompatible with non-Abelian gauge theory if local color charge density is non-zero. Instead, the equation of state becomes dependent on u mu via modes which are roughly equivalent to ghost modes in the hydrodynamic limit. These modes can be physically imagined as a field of "purcell swimmers" whose "arms and legs" are outstretched in Gauge space. Also, vorticity should couple to the Wilson loop via the chromo--electro-magnetic field tensor, which in local equilibrium is not a "force" but instead represents the polarization tensor of the gluons. We show that because of this coupling vorticity also acquires swirling non-hydrodynamic modes. We then argue that these swirling and swimming non-hydrodynamic modes are the manifestation of gauge redundancy within local equilibrium, and speculate on their role in quark-gluon plasma thermalization.

EUROPEAN PHYSICAL JOURNAL A 56[4], 121, 2020. DOI: 10.1140/epja/s10050-020-00121-z

[P139-2020] "The Use of Films of Multilayer Graphene as Coatings of Light-Emitting GaAs Structures"

Alaferdov, A. V.*; Vikhrova, O. V.; Danilov, Yu. A.; Zvonkov, B. N.; Moshkalev, S. A.

A significant (almost two orders of magnitude) increase in the intensity of photo- and electroluminescence of a diode structure with an InGaAs/GaAsSb/GaAs quantum well, GaMnAs layer as a spin injector, and contact coating of a multilayer graphene film has been experimentally detected. The result has been explained by the possible formation of a hybrid system of multilayer graphene and GaAs semiconductor under the influence of He-Ne laser radiation, which leads to a change in the band diagram of the heterostructure.

OPTICS AND SPECTROSCOPY 128[3], 387-394, 2020. DOI: 10.1134/S0030400X20030030

[P140-2020] "Treatment of aqueous solutions of 1,4-dioxane by ozonation and catalytic ozonation with copper oxide (CuO)"

Scaratti, G.; Basso, A.; **Landers, R.***; Alvarez, P. J. J.; Li Puma, G.; Moreira, R. F. P. M.

In this study, treatment for the removal of 1,4-dioxane by ozone and by catalytic ozonation using CuO as the catalyst was investigated. While the removal of 1,4-dioxane was small (20%) and mineralization negligible after 6 h of ozonation treatment, the removals of 1,4-dioxane and total organic carbon increased by factors of 10.35 and 81.25, respectively, after catalytic ozonation in the presence of CuO. The mineralization during catalytic ozonation was favoured at pH 10 (94.91 min(-1)), although it proceeded even at pH 3 (54.41 min(-1)). The CuO catalyst decreased the equilibrium concentration of soluble ozone and favoured its decomposition to reactive oxidative species. Radical scavenging experiments demonstrated that superoxide radicals were the main species responsible for the degradation of 1,4-dioxane. Further scavenging experiments with phosphate confirmed the presence of Lewis active sites on the surface of CuO, which were responsible for the adsorption and decomposition of ozone. The reaction mechanism proceeded through the formation of ethylene glycol diformate, which quickly hydrolyzed to ethylene glycol and formic acid as intermediate products. The stability of CuO indicated weak copper leaching and high catalytic activity for five recycling cycles. The toxicity of the water, assessed by Vibrio fischeri bioluminescence assays, remained the same (low toxicity) after catalytic ozonation while it increased after treatment with ozonation alone.

ENVIRONMENTAL TECHNOLOGY 41[11], 1464-1476, 2020. DOI: 10.1080/09593330.2018.1538259

[P141-2020] "Underlying event properties in pp collisions at root s=13 TeV"

Acharya, S.; Acosta, F. T.; Adam, J.; **Albuquerque, D. S. D.*; Chinellato, D. D.*; De Souza, R. D.*; Takahashi, J.***; et. al.; ALICE Collaboration

This article reports measurements characterizing the Underlying Event (UE) associated with hard scatterings at midrapidity (|eta| < 0.8) in pp collisions at <mml:msqrt>s = 13 TeV. The hard scatterings are identified by the leading particle, the charged particle with the highest transverse momentum (pTleading) in the event. Charged-particle number-densities and summed transverse-momentum densities are measured in different azimuthal regions defined with respect to the leading particle direction: Toward, Transverse, and Away. The Toward and Away regions contain the fragmentation products of the hard scatterings in addition to the UE contribution, whereas particles in the Transverse region are expected to originate predominantly from the UE. The study is performed as a function of pTleading with three different p(T) thresholds for the associated particles, pTtrack > 0.15, 0.5, and 1.0 GeV/c. The charged-particle density in the Transverse region rises steeply for low values of pTleading and reaches a plateau. The results confirm the trend that the charged-particle density in the Transverse region shows a stronger increase with s than the inclusive charged--particle density at midrapidity. The UE activity is increased by approximately 20% when going from 7 TeV to 13 TeV pp collisions. The plateau in the Transverse region (5 <pTleading< 40 GeV/c) is further characterized by the probability distribution of its charged-particle multiplicity normalized to its average value (relative transverse activity, R-T) and the mean transverse momentum as a function of R-T. Experimental results are compared to model calculations using PYTHIA 8 and EPOS LHC. The overall agreement between models and data is within 30%. These measurements provide new insights on the interplay between hard scatterings and the associated UE in pp collisions.

JOURNAL OF HIGH ENERGY PHYSICS 4[192], 2020. DOI: 10.1007/JHEP04(2020)192

[P142-2020] "Unveiling the Origin of the Giant Barocaloric Effect in Natural Rubber"

Miliante, C. M.; Christmann, A. M.; Usuda, E. O.; Imamura, W.; **Paixao, L. S.*;** Carvalho, A. M. G.; Muniz, A. R.

The barocaloric effect (BCE) is characterized as thermal responses (variations of temperature or entropy) in a material resulting from compression. Several materials exhibit a BCE suitable for development of solid-state cooling devices, typically associated with pressure-induced phase transitions. A giant BCE has been observed for natural rubber (NR), which makes it a cheap and environmentally friendly candidate for such a purpose. The reason for the significant BCE in NR is still elusive, considering that there is no evidence of phase transitions in the process. The present study uses a combination of classical molecular dynamics (MD) simulations and a thermodynamic analysis to investigate the origin of the giant BCE in NR. MD simulations of adiabatic compression cycles for NR were carried out under varied applied pressures and initial temperatures and were able to capture the BCE. A detailed analysis of the results helped us to elucidate the structural transformations and resulting energy changes in the material under compression. MD results for isothermal compression along with the thermodynamic analysis showed that the high compressibility of NR combined with an unusual decrease in the potential energy at the molecular level upon compression favors significantly the BCE (quantified by isothermal entropy changes and adiabatic temperature changes in the process), a feature not commonly seen in other materials. These findings can be extended to other polymers and are certainly going to be useful toward the design of materials with an enhanced BCE.

MACROMOLECULES 53[7], 2606-2615, 2020. DOI: 10.1021/acs.macromol.0c00051

[P143-2020] "Weak ferromagnetic component in goethite (alpha-FeOOH) and its relation with microstructural characteristics"

Valezi, D. F.; Carneiro, C. E. A.; Costa, A. C. S.; Paesano Jr, A.; Spadotto, J. C.; Solorzano, I. G.; **Londono, O. M.*;** Di Mauro, E.

Goethite is an antiferromagnetic material that frequently presents a superimposed weak ferromagnetic component. In this research, two goethite samples were prepared using distinct synthesis routes, being later subjected to heat treatment. Magnetization dynamics were analyzed as a function of applied magnetic field and temperature. Moreover, the magnetic measurements were correlated with the resulting microstructures, obtained through scanning and transmission electron microscopy. The results indicate an enhanced ferromagnetic behavior in those goethite samples, with greater presence of defects and imperfections. Besides that, it was observed a reduction of magnetic fluctuations after the healing of the samples via heat treatment. Despite what is vastly proposed in the literature to explain the origin of the magnetic component in goethite, our analysis showed that, for the studied samples, this effect is caused by a magnetic mismatch in the antiferromagnetic lattice. This mismatch is possibly caused by defects as grain boundaries, voids and grain rotations, which may lead to dislocations and consequently to magnetic mismatches in the lattice.

MATERIALS CHEMISTRY AND PHYSICS 246[122851], 2020. DOI: 10.1016/j.matchemphys.2020.122851

[P144-2020] "Zeolite-templated Carbon Network: A Beta Zeolite Case Study"

Oliveira, E. F.*; Machado, L. D.; Baughman, R. H.; **Galvao, D. S.***

In this work, we report a preliminary study, based on molecular dynamics simulations, about 3D carbon nanotube networks that could be formed inside the beta zeolites.

We investigated their structural stability and mechanical properties. Our results show that from all possible carbon nanotubes that can be embedded inside the channels of the beta zeolite, the one with chirality (6,0) is the most stable. Using the carbon nanotube (6,0), it is possible to build 3D structures with both all (higher density) and only partially (lower density) filled zeolite channels. Under tensile uniaxial force, the 3D low-density carbon nanotube networks are anisotropic and can be stretched along the direction in which all nanotubes are perpendicular up to 130% of strain without fracture. Also, the porosity and network stiffness can be tuned depending on the amount of carbon nanotubes filling the channels of the zeolites.

MRS ADVANCES 5[14-15][SI], 751-756, 2020. DOI: 10.1557/adv.2020.183

Patentes do IFGW

[Pa001-2020] "Vibrômetro laser doppler rms"

Jaime Frejlich Sochaczewsky*; Antonio Carlos da Costa; Agnaldo Aparecido Freschi; José Roberto de França Arruda

Número da Patente ou Registro: Agência INOVA PI0303986-2
Tipo: Patente de Invenção
Mês/Ano de Conclusão: 01/2020 - INPI/BBRASIL

***Autores da comunidade IFGW**
Fonte: Web of Science on-line (WOS)

Defesas de Dissertações do IFGW

[D007-2020] "Relaxações causais e não-localidade quântica em sistemas multipartidos"
Aluno: Gabriel Pereira Alves
Orientador: Prof. Dr. Rafael Luiz da Silva Rabelo
Data: 21/05/2020

[D008-2020] "Caracterização Cristalográfica de Nanopartículas utilizando Função de Distribuição de Pares (PDF) derivada de Difração de Elétrons com Precessão (PED)"
Aluno: Leonardo Marcon Corrêa
Orientador: Prof. Dr. Daniel Mario Ugarte
Data: 01/06/2020

[D009-2020] "Estudo de propriedades termoelétricas do semicondutor As(2)Se(3) através de cálculos ab initio"
Aluno: Murilo Aguiar da Silva
Orientador: Prof. Dr. Alex Antonelli
Data: 05/06/2020

[D010-2020] "Efeitos de desordem em modelos tipo Kitaev"
Aluno: Yago Barbosa de Godoy
Orientador: Prof. Dr. Eduardo Miranda
Data: 08/06/2020

Defesas de Teses do IFGW

[T007-2020] "Simulações atomísticas de líquidos formadores de vidros: uma aplicação a ligas metaestáveis de Cu-Zr(Al)"
Aluno: René Alberto Alvarez Donado
Orientador: Prof. Dr. Alex Antonelli
Data: 29/05/2020

Fonte: Portal IFGW/Pós-graduação - Agenda de Colóquios, Defesas e Seminários.
Disponível em: http://portal.ifi.unicamp.br/pos-graduacao

Defesas de Teses do PECIM

[Pe002-2020] "Os itens de física do ENEM classificados por análise fatorial exploratória"
Aluno: Renato Pacheco Villar
Orientador: Prof. Dr. Mauricio Urban Kleinke
Data: 29/05/2020

[Pe003-2020] "Concepções de estudantes sobre as atividades experimentais no ensino de Física: um estudo a partir da exposição Veja a luz como nunca viu"
Aluno: Antonio Marcos de Souza
Orientador: Prof. Dr. José Joaquin Lunazzi
Data: 27/05/2020

Fonte: Página do PECIM - Programa de Pós-Graduação Multiunidades em Ensino de Ciências e Matemática – Mestrado e Doutorado (PECIM) da Unicamp.
Disponível em: https://www.pecim.unicamp.br/bancas

Abstracta

Instituto de Física
Diretor: Prof. Dr. Pascoal José Giglio Pagliuso
Diretora Associada: Profa. Dra. Mônica Alonso Cotta
Universidade Estadual de Campinas - UNICAMP
Cidade Universitária Zeferino Vaz
13083-859 - Campinas - SP - Brasil
e-mail: secdir@ifi.unicamp.br
Fone: +55 19 3521-5300

Publicação

Biblioteca do Instituto de Física Gleb Wataghin
http://portal.ifi.unicamp.br/biblioteca

Diretora Técnica: Sandra Maria Carlos Cartaxo
Coordenadora da Comissão de Biblioteca: Profa. Dra. Arlene Cristina Aguilar

Elaboração:
Maria Graciele Trevisan (Bibliotecária)
Ayres Neri da Cunha Junior (Técnico Administrativo)
contato: infobif@ifi.unicamp.br